Journal of Sound and Vibration (2001) **241**(5), 895–912
doi:10.1006/jsvi.2000.3339, available online at http://www.idealibrary.com on IDEAL®

NUMERICAL ANALYSIS OF INTERNAL COMBUSTION ENGINE INTAKE NOISE WITH A MOVING PISTON AND A VALVE

Y. S. Kim and D. J. Lee

Department of Aerospace Engineering, Korea Advanced Institute of Science and Technology, 373-1, *Kusong-dong, Yusong-gu, Taejon* 305-701, *Korea. E-mail: djlee@mail.kaist.ac.kr*

(*Received* 21 *July* 1999, *and in final form* 21 *September* 2000)

Traditionally, intake noise from internal combustion engine has not received much attention compared to exhaust noise. But nowadays, the intake noise is a major contributing factor to automotive passenger compartment noise levels. The main objective of this paper is to identify the mechanism of generation, propagation and radiation of the intake noise. With a simple geometric model, it is found that one of the main noise sources for the intake stroke is the pressure surge, which is a compression wave due to the compressed air near the intake valve after closing. The pressure surge, which has the non-linear acoustic behavior, propagates and radiates with relatively large amplitude. In this paper, unsteady compressible Navier–Stokes equations are employed for the intake stroke of axisymmetric model having a single moving piston and a single moving intake valve. To simulate the periodic motion of the piston and the valve, unsteady deforming mesh algorithm is employed. For the purpose of perfect closing of the intake valve, the numbers of mesh are changed using a Lagrange interpolation. In order to resolve the small amplitude waves at the radiation field, essentially non-oscillatory (ENO) schemes are used. The source of the intake noise can be identified through the visualization of propagation in a finite duct and radiation to the far fields. Comparison with measured data is given for in-duct pressure showing a better agreement than the one-dimensional calculation data.

1. INTRODUCTION

Recently, an intake noise, which was a relatively minor noise source in the past, has rapidly become a noticeable one as automotive passengers who prefer a higher performance and lower noise automobile increase. Particularly, the intake noise is closely related to engine performance. Therefore, it is necessary to investigate in detail the noise source related to fluid fluctuations caused by dynamic characteristics of the real engine.

Bender and Brammer [1] wholly described external radiation due to both intake and exhaust noise. Nishio *et al.* [2] newly developed air intake system testing apparatus, called the PULSATION SIMULATOR. Generally, in the past, development of the intake system was conducted by giving priority to engine volumetric efficiency. However, by using this apparatus, they tried to apply low noise intake system to an early stage of engine development in parallel with the study of volumetric efficiency. Jones [3] has determined the radiated exhaust noise by modelling of the full non-linear unsteady exhaust gas flow in that the linear acoustic analysis of exhaust system is limited for only a few cases. Evidence of non-linear acoustic behavior of the intake noise was found by Lamancusa and Todd [4] who predicted the intake noise source by experiment. It was reported that the large acoustic

0022-460X/01/150895 + 18 $35.00/0

pressure fluctuations over 7 kPa peak to peak at the intake valve invoke the possibility of non-linear acoustic effects. As the non-linear wave propagates through the duct, considerable wave steepening occurs.

Most of the work reported in intake and exhaust system is related to the use of the method of characteristics or the one-dimensional non-linear flow calculations. Payri [5] solved the one-dimensional flow equations in the case of the exhaust system of a single-cylinder engine by using MacCormack predictor–corrector schemes. He concluded that this scheme is low dispersive and it shows less numerical oscillations when subject to sudden changes in the flow conditions, which may be a critical feature when considering the flow in I.C. engine exhaust system.

Apart from the finite difference schemes, the finite volume method is broadly used for multi-dimensional flow calculations. The method takes full advantage of an arbitrary mesh, where a large number of options are open for the definition of the control volumes around which the conservation laws are expressed. By the direct discretization of the integral form of the conservation laws it can be ensured that the basic quantities mass, momentum and energy will also remain conserved at the discrete level. In the present paper, the finite volume method with a spatially high accuracy ENO (essentially non-oscillatory) scheme is applied to the axisymmetric equations in the generalized co-ordinates.

Generally, owing to the complex geometry of intake and exhaust system the source term that is arisen from the flow is obtained by experiment and only the acoustic field is solved with the source term in most cases. But as the computer is developed rapidly, the fluid and the acoustic fields can be solved directly by using computational aeroacoustics (CAA) technique. An attempt to apply the ENO schemes to aeroacoustic problems was made by Meadow *et al.* [6], who discussed spurious entropy waves in calculations of unsteady shock in the flow field. Yang [7] developed the new Lagrangian ENO interpolation of the third order accuracy. Ko and Lee [8] improved the fourth order modified flux approach ENO scheme of high resolution and high order. The ENO schemes used in this paper not only produce sharp shock profiles but also resolve the small amplitude waves.

At the radiation fields, Thomson's non-reflecting characteristic-based boundary condition was used as the physical boundary conditions because inward propagating waves in order not to contaminate the acoustic fields.

In the present paper, a single moving piston and a single moving valve is used to investigate the major intake noise source during intake stroke. Usually, the moving mesh used to solve the multi-dimensional problem keeps the number of the mesh and could not achieve the perfect closing of the valve. The important improvement in this paper is that using a Lagrange interpolation can change the numbers of mesh, and so can help in simulating the motion of the perfect closing of the valve. A comparison is given between the present calculated data and measured data [9] for in-duct pressure with satisfactory results.

2. GOVERNING EQUATIONS

The conservative forms of unsteady compressible axisymmetric Navier–Stokes equations in generalized co-ordinates are considered in this paper as follows:

$$\frac{\partial \hat{Q}}{\partial t} + \frac{\partial \hat{F}}{\partial \xi} + \frac{\partial \hat{G}}{\partial \eta} + \alpha \hat{H} = \frac{1}{\mathrm{Re}} \left(\frac{\partial \hat{F}_v}{\partial \xi} + \frac{\partial \hat{G}_v}{\partial \eta} + \alpha \hat{H}_v \right), \tag{1}$$

where

$$\hat{Q} = \frac{1}{J}\begin{vmatrix} \rho \\ \rho u \\ \rho v \\ \rho e_t \end{vmatrix}, \quad \hat{F} = \frac{1}{J}\begin{vmatrix} \rho U \\ \rho u U + p\xi_x \\ \rho v U + p\xi_y \\ (\rho e_t + p)U - p\xi_t \end{vmatrix}, \quad \hat{G} = \frac{1}{J}\begin{vmatrix} \rho V \\ \rho u V + p\eta_x \\ \rho v V + p\eta_y \\ (\rho e_t + p)V - p\eta_t \end{vmatrix},$$

$$\hat{H} = \frac{1}{J}\frac{1}{y}\begin{vmatrix} \rho v \\ \rho u v \\ \rho v^2 \\ (\rho e_t + p)v \end{vmatrix},$$

$$\hat{F}_v = \frac{1}{J}[\xi_x F_v + \xi_y G_v], \quad \hat{G}_v = \frac{1}{J}[\eta_x F_v + \eta_y G_v], \quad \hat{H}_v = \frac{H_v}{J}. \tag{2}$$

The axisymmetric and two-dimensional equations are formulated in the case of $\alpha = 1$ and 0 respectively. $\hat{F}_v, \hat{G}_v, \hat{H}_v$ are related to viscous diffusion terms. U and V are contravariant velocity components of the x, y directions, respectively, and can be expressed as follows:

$$U = \xi_t + \xi_x u + \xi_y v, \qquad V = \eta_t + \eta_x u + \eta_y v. \tag{3}$$

3. NUMERICAL METHOD

3.1. THE ENO SCHEMES IN MOVING CO-ORDINATES

By using third order Upwind-ENO schemes of Harten's flux difference splitting type, the numerical flux term at the boundary surface is formulated as follows [10]:

$$\tilde{F}_{i+1/2,j} = \frac{1}{2}[\hat{F}_{i,j} + \hat{F}_{i+1,j} + R_{i+1/2,j}\Phi^{ENO3}_{i+1/2,j}/J_{i+1/2,j}]. \tag{4}$$

The components of the column vector $\Phi^{ENO3}_{i+1/2}$ (we will omit j index from now) and corrected propagation speed of the characteristic value, $\gamma'_{i+1/2}$ are given as

$$\phi^{l(ENO3)}_{i+1/2} = g^l_{i+1}(a^l_{i+1/2}) + g^l_i(a^l_{i+1/2}) - \Psi(\gamma^l_{i+1/2})\Delta_+ w^l_i, \tag{5}$$

$$\gamma^l_{i+1/2} = \begin{cases} a^l_{i+1/2} + \{g^l_{i+1}(a^l_{i+1/2}) - g^l_i(a^l_{i+1/2})\}/\Delta_+ w^l_i & \text{if } \Delta_+ w^l_i \neq 0, \\ 0 & \text{otherwise} \end{cases} \tag{6}$$

and

$$\Psi(z) = \begin{cases} |z| & \text{if } |z| \geqslant \varepsilon, \\ (z^2 + \varepsilon^2)/2\varepsilon & \text{if } |z| < \varepsilon, \end{cases} \tag{7}$$

where l represents four characteristic waves in the case of two dimensions and Δ_+ is the forward difference. $\Psi(z)$ is an entropy correction function and is usually applied to the genuinely non-linear eigenvalues, and ε is selected as some small number. In our study, $\Psi(z)$ was used $|z|$ only because the characteristic of the intake noise is softly non-linear. In

equation (5), g^l is a limiter function that determines the essentially non-oscillatory characteristics. In the case of third order accuracy g^l is given as

$$g_i^l = \sigma(a_{i+1/2}^l)\beta_i^l + \tilde{\sigma}(a_{i+1/2}^l)\tilde{\beta}_i^l + \hat{\sigma}(a_{i+1/2}^l)\hat{\beta}_i^l, \tag{8}$$

$$\beta_i^l = m(\Delta_- w_i^l, \Delta_+ w_i^l),$$

$$\tilde{\beta}_i^l = m(\Delta_-\Delta_- w_{i,}^l \Delta_-\Delta_+ w_i^l), \quad \hat{\beta}_i^l = 0 \quad \text{if } (|\Delta_- w_i^l| \leqslant |\Delta_+ w_i^l|), \tag{9}$$

$$\hat{\beta}_i^l = m(\Delta_-\Delta_+ w_{i,}^l \Delta_+\Delta_+ w_i^l), \quad \tilde{\beta}_i^l = 0 \quad \text{otherwise}$$

and

$$\sigma(a_{i+1/2}^l) = |a_{i+1/2}^l|(1 - |\lambda a_{i+1/2}^l|)/2,$$

$$\tilde{\sigma}(a_{i+1/2}^l) = a^+(2 - 3|\lambda a_{i+1/2}^l| + |\lambda a_{i+1/2}^l|^2)/6 + a^-(-1 + |\lambda a_{i+1/2}^l|^2)/6, \tag{10}$$

$$\hat{\sigma}(a_{i+1/2}^l) = a^+(-1 + |\lambda a_{i+1/2}^l|^2)/6 + a^-(2 - 3|\lambda a_{i+1/2}^l| + |\lambda a_{i+1/2}^l|^2)/6,$$

where λ is the mesh ratio ($\Delta t/\Delta x$) and superscripts $+$ and $-$ represent positive- and negative-running waves, $a_{i+1/2}^l > 0$ and $a_{i+1/2}^l < 0$ respectively. The minmod function $m(x, y)$ is obtained as

$$m(a, b) = \begin{cases} \text{sign}(a) \times \min(|a|, |b|), & a \times b \geqslant 0, \\ 0 & \text{otherwise.} \end{cases} \tag{11}$$

The characteristic variables, Δw_i^l and propagation speeds, $a_{i+1/2}^l$ in equation (6) are represented as

$$\delta W = \begin{bmatrix} \delta\bar{\rho} - \dfrac{1}{\bar{c}^2}\delta\bar{p} \\ \delta\tilde{V} \\ (\delta\bar{p} + \overline{\rho c}\delta\tilde{U})/2\bar{c}^2 \\ (\delta\bar{p} - \overline{\rho c}\delta\tilde{U})/2\bar{c}^2 \end{bmatrix}, \quad a_{i+1/2}^l(\text{diagonal}) = \begin{bmatrix} \bar{U} \\ \bar{U} \\ \bar{U} + \bar{c}\sqrt{\xi_x^2 + \xi_y^2} \\ \bar{U} - \bar{c}\sqrt{\xi_x^2 + \xi_y^2} \end{bmatrix}, \tag{12}$$

where the mean contravarient velocity and the contravarient's differentials are given as

$$\bar{U} = \xi_t + \xi_x\bar{u} + \xi_y\bar{v}, \quad \delta\tilde{U} = \tilde{\xi}_x\delta u + \tilde{\xi}_y\delta v, \quad \delta\tilde{V} = -\tilde{\xi}_x\delta v + \tilde{\xi}_y\delta u, \tag{13}$$

$$\tilde{\xi}_x = \frac{\xi_x}{\sqrt{\xi_x^2 + \xi_y^2}}, \quad \tilde{\xi}_y = \frac{\xi_y}{\sqrt{\xi_x^2 + \xi_y^2}},$$

and the mean values in equations (12) and (13) are obtained by Roe average defined as

$$\bar{\rho} = \sqrt{\rho_i\rho_{i+1}}, \qquad \bar{u} = \frac{u_i\sqrt{\rho_i} + u_{i+1}\sqrt{\rho_{i+1}}}{\sqrt{\rho_i} + \sqrt{\rho_{i+1}}}, \qquad \bar{v} = \frac{v_i\sqrt{\rho_i} + v_{i+1}\sqrt{\rho_{i+1}}}{\sqrt{\rho_i} + \sqrt{\rho_{i+1}}}, \tag{14}$$

$$\bar{h} = \frac{h_i\sqrt{\rho_i} + h_{i+1}\sqrt{\rho_{i+1}}}{\sqrt{\rho_i} + \sqrt{\rho_{i+1}}}, \qquad \bar{c}^2 = (\gamma - 1)(\bar{h} - 1/2 \times (\bar{u}^2 + \bar{v}^2)).$$

The right-hand characteristic matrix $R_{i+1/2}$ in equation (4) and its constituting variables are

$$R_{i+1/2} = \begin{bmatrix} 1 & 0 & 1 & 1 \\ \bar{u} & \bar{\rho}\tilde{\xi}_y & \bar{u} + \bar{c}\tilde{\xi}_x & \bar{u} - \bar{c}\tilde{\xi}_x \\ \bar{v} & -\bar{\rho}\tilde{\xi}_x & \bar{v} + \bar{c}\tilde{\xi}_y & \bar{v} - \bar{c}\tilde{\xi}_y \\ 1/2(\bar{u}^2 + \bar{v}^2) & \bar{\rho}(\bar{u}\tilde{\xi}_y - \bar{v}\tilde{\xi}_x) & \bar{H} + \bar{c}(\bar{u}\tilde{\xi}_x + \bar{v}\tilde{\xi}_y) & \bar{H} - \bar{c}(\bar{u}\tilde{\xi}_x + \bar{v}\tilde{\xi}_y) \end{bmatrix}. \quad (15)$$

3.2. CREATING AND REMOVING MESH ALGORITHM WITH A LAGRANGE INTERPOLATION

For the simulation of perfect closing of the intake valve, creating and removing mesh algorithm must be accompanied with appropriate interpolation that minimizes interpolation error. In this study, third order Lagrange interpolation is used, which is a basis of ENO interpolation. The Lagrange interpolating polynomial is simply a reformulation of the Newton polynomial that avoids the computation of divided difference. It can be represented concisely as

$$Q(x) = \sum_{i=0}^{n} L_i Q(x_i), \quad L_i(x) = \prod_{\substack{j=0 \\ j \neq i}}^{n} \frac{x - x_j}{x_i - x_j}, \quad (16)$$

where Q represents interpolating variables and Π designates the "product of". For the third order accuracy, four mesh points and four flow variables are required. In this paper, conservative variables $[\rho, \rho u, \rho v, \rho e_t]$ are interpolated as in the following procedure.

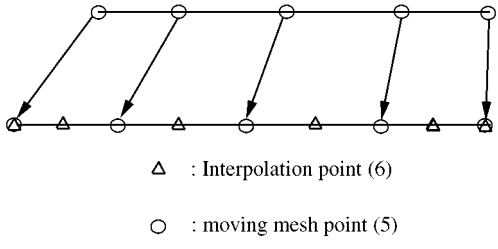

First, using a deforming mesh algorithm, mesh point moves to the next position and then mesh system is regenerated adding one mesh point. Second, keeping the boundary values, new mesh points are interpolated by using moving mesh point's values.

3.3. TIME INTEGRATION METHOD

The diagonally implicit approximate factorization (DIAF) method introduced by Pulliam [11] was used for time integration but it has a problem for accurate unsteady calculation since it has first order accuracy of the δ-form. Therefore, Matuno's [12] δ^k-correction method was employed to settle this problem. This method is able to have arbitrary time accuracy for variable time step, and is to be used for any type of the spatial derivative method. In this paper, δ^k-correction method with third order time accuracy is used.

3.4. NON-REFLECTING CHARACTERISTIC BOUNDARY CONDITION

Thompson's [13, 14] characteristics-based boundary condition was used as the physical boundary conditions. At the inlet and outlet numerical boundaries of the $\xi =$ constant, waves are able to be considered as one dimension:

$$\partial_{\tau\xi}\hat{Q} + \partial_{\xi}\hat{F} = 0. \tag{17}$$

Equation (17) can be presented by using characteristic variable at $\xi =$ constant boundary, and this can be decomposed as incoming and outgoing waves depending on the characteristic value $\hat{\Lambda}$'s sign as shown below

$$\partial_{\tau\xi}\hat{W}|_{out} + \hat{\Lambda}|_{out}\partial_{\xi}\hat{W} = 0, \quad \partial_{\tau\xi}\hat{W}|_{in} + \hat{\Lambda}|_{in}\partial_{\xi}\hat{W} = 0. \tag{18}$$

For non-reflecting condition, $\hat{\Lambda}|_{in}$ must be zero and the characteristic value entering from the boundary must not change as time passes. Therefore, equations (18) are formulated as follows:

$$\partial_{\tau\xi}\hat{W}|_{out} = -\hat{\Lambda}|_{out}\partial_{\xi}\hat{W}, \qquad \partial_{\tau\xi}\hat{W}|_{in} = 0. \tag{19}$$

By considering equation (17), the local one-dimensional inviscid (LODI) system can be obtained at each point on the boundary. The LODI system can be cast in many different forms depending on the choice of variable [13]. In terms of primitive variables, the LODI system is represented as follows:

$$\begin{aligned}
&\frac{\partial}{\partial t}\left(\frac{\rho}{J}\right) + \frac{\rho}{\sqrt{2}c}(L_3 + L_4) + L_1 = 0,\\
&\frac{\partial}{\partial t}\left(\frac{p}{J}\right) + \frac{\rho c}{\sqrt{2}}(L_3 + L_4) = 0,\\
&\frac{\partial}{\partial t}\left(\left(\frac{1}{\rho c}\frac{\partial}{\partial \xi}\left(\frac{p}{J}\right) + \left(\tilde{\xi}_x\frac{\partial}{\partial \xi}\left(\frac{u}{J}\right) + \tilde{\xi}_y\frac{\partial}{\partial \xi}\left(\frac{v}{J}\right)\right)\right)\Big/ J\right) + L_2 = 0,\\
&\frac{\partial}{\partial t}\left(\left(\frac{1}{\rho c}\frac{\partial}{\partial \xi}\left(\frac{p}{J}\right) - \left(\tilde{\xi}_x\frac{\partial}{\partial \xi}\left(\frac{u}{J}\right) + \tilde{\xi}_y\frac{\partial}{\partial \xi}\left(\frac{v}{J}\right)\right)\right)\Big/ J\right) + \frac{1}{\sqrt{2}}(L_3 - L_4) = 0.
\end{aligned} \tag{20}$$

The resulting equations are easy to interpret and allow us to infer values for the wave amplitude variations by considering the flow locally as inviscid and one-dimensional. The relations obtained by this idea are not physical boundary conditions exactly but should be viewed as compatibility relations between the choices made for the physical boundary conditions and the amplitudes of waves crossing the boundary [15]. Considering subsonic outflow boundary conditions, one can notice that three characteristic waves, L_1, L_2 and L_3 leave the computational domain while one of them L_4 enters it at the speed of λ_4. For non-reflecting conditions, the incoming wave L_4 must be zero and the other three L_i' are computed from interior points as follows:

$$L_1 = (u\xi_x + v\xi_y)\left(\frac{\partial}{\partial \xi}\left(\frac{\rho}{J}\right) - \frac{1}{c^2}\frac{\partial}{\partial \xi}\left(\frac{p}{J}\right)\right),$$

$$L_2 = (u\xi_x + v\xi_y)\left(\tilde{\xi}_y\frac{\partial}{\partial \xi}\left(\frac{u}{J}\right) - \tilde{\xi}_x\frac{\partial}{\partial \xi}\left(\frac{v}{J}\right)\right),$$

$$L_3 = (u\xi_x + v\xi_y + c\sqrt{\xi_x^2 + \xi_y^2})\left(\frac{1}{\rho c}\frac{\partial}{\partial \xi}\left(\frac{p}{J}\right) + \left(\tilde{\xi}_x \frac{\partial}{\partial \xi}\left(\frac{u}{J}\right) + \tilde{\xi}_y \frac{\partial}{\partial \xi}\left(\frac{v}{J}\right)\right)\right)\frac{1}{\sqrt{2}},$$

$$L_4 = (u\xi_x + v\xi_y - c\sqrt{\xi_x^2 + \xi_y^2})\left(\frac{1}{\rho c}\frac{\partial}{\partial \xi}\left(\frac{p}{J}\right) - \left(\tilde{\xi}_x \frac{\partial}{\partial \xi}\left(\frac{u}{J}\right) + \tilde{\xi}_y \frac{\partial}{\partial \xi}\left(\frac{v}{J}\right)\right)\right)\frac{1}{\sqrt{2}}. \quad (21)$$

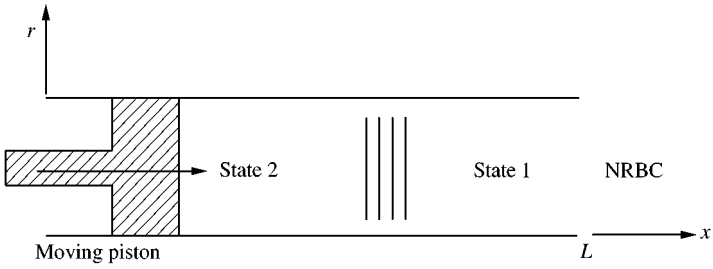

Figure 1. Schematic diagram and co-ordinate of a uniform duct with a moving piston.

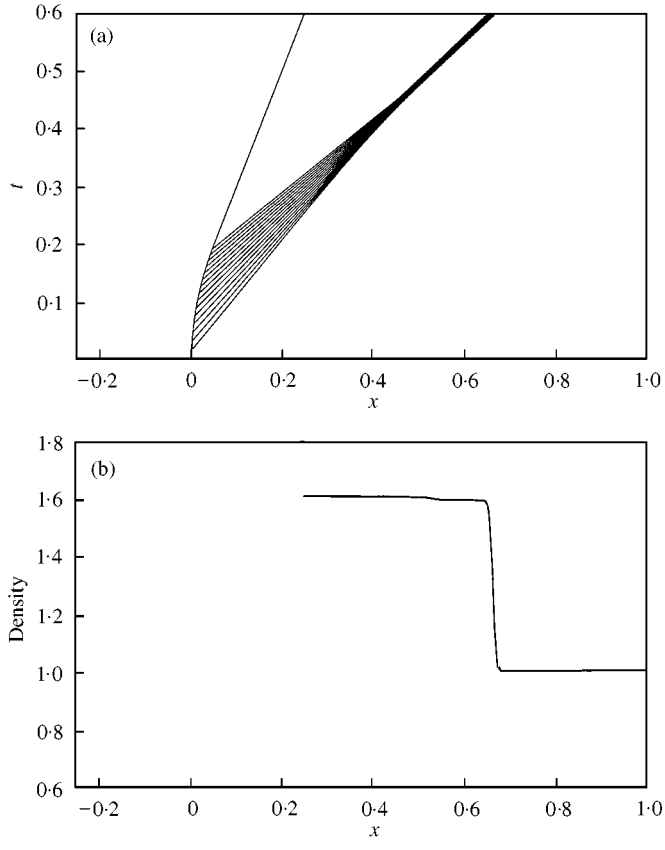

Figure 2. (a) Compressive finite wave. (b) Spatial distribution of the density in two different cases: ———, non-interpolation; · · · · · ·, Lagrange interpolation.

4. VALIDATION

4.1. MOVING PISTON

For the validation of deforming mesh algorithm with a Lagrange interpolation, we solved the moving piston problem. Figure 1 shows the schematic diagram and co-ordinate system of a uniform duct with a moving piston. Mesh system is 201×11 and non-dimensional time step, Δt is 0·001. Figure 2 represents a compressive finite wave that the piston accelerates (non-dimensional acceleration speed, $a_p = 2{\cdot}5$) first to the right and then moves with a constant velocity (non-dimensional velocity, $u_p = 0{\cdot}5$). The domain of calculation is changed but numbers of mesh are kept constant as time passes. Figure 2(a) shows the pressure contour of compression wave developing to shock wave. Figure 2(b) shows a comparison of the deforming mesh calculation only and calculation with removing mesh points through the Lagrange interpolation. Thirty mesh points are removed at the non-dimensional time of 0·6. Figure 3(a) represents expansion waves orginated from deceleration of the piston. As shown in Figures 2(b) and 3(b), it seems that the removing–creating mesh algorithm with Lagrange interpolation is suitably applied to the motion of the piston.

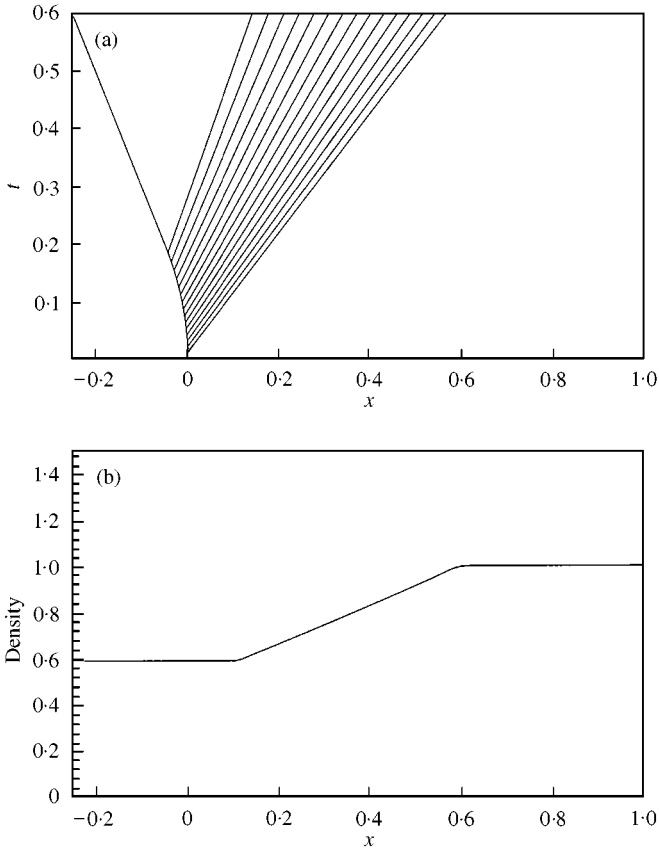

Figure 3. (a) Centered expansion wave. (b) Spatial distribution of the density in two different cases: ———, non-interpolation; · · · · · ·, Lagrange interpolation.

4.2. RADIATION OF THE LINEAR ACOUSTIC WAVE (BAFFLE PROBLEM)

The linear acoustic wave propagation and radiation due to a vibrating piston is simulated in axisymmetric co-ordinates to simulate the radiated acoustic field from the intake duct system. The conservative forms of axisymmetric Euler equations are used for the computations. For the present work, improved characteristic radiation boundary conditions are used for non-reflecting acoustic radiation. On the radiation boundary, the free-field impedance conditions are imposed to obtain the fluctuations of velocity and pressure, while the density is evaluated by Thomson's characteristic non-reflecting boundary conditions as follows:

$$u'_{radial} = \frac{a_0}{\rho_0}\rho', \qquad p' = a_0^2\rho', \tag{22}$$

where ρ', p' and u'_{radial} are the fluctuations of density, pressure and radial velocity, respectively (ρ_0 and a_0 are the ambient density and the speed of sound respectively) [16]. These relations are used as the non-reflecting radiation boundary conditions for the present computations in accordance with the density fluctuation obtained by Thomson's non-reflecting boundary conditions.

The schematic diagram is described in Figure 4. A grid system of 100×100 is used. The results of computations by the third order accuracy ENO(ENO3) schemes are presented in Figure 5. It is shown that the numerical solutions are in good agreement with the analytic solutions. The acoustic waves are radiated well through the farfield boundaries with little reflecting waves and propagated well along the inviscid wall keeping the wave fronts undistorted.

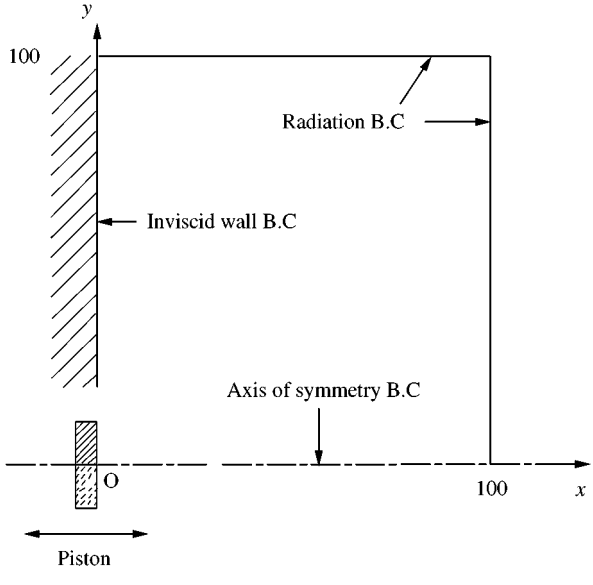

Figure 4. Schematic diagram for the linear acoustic wave radiation problem: piston velocity $u = 10^{-4}\sin(\pi t/5)$.

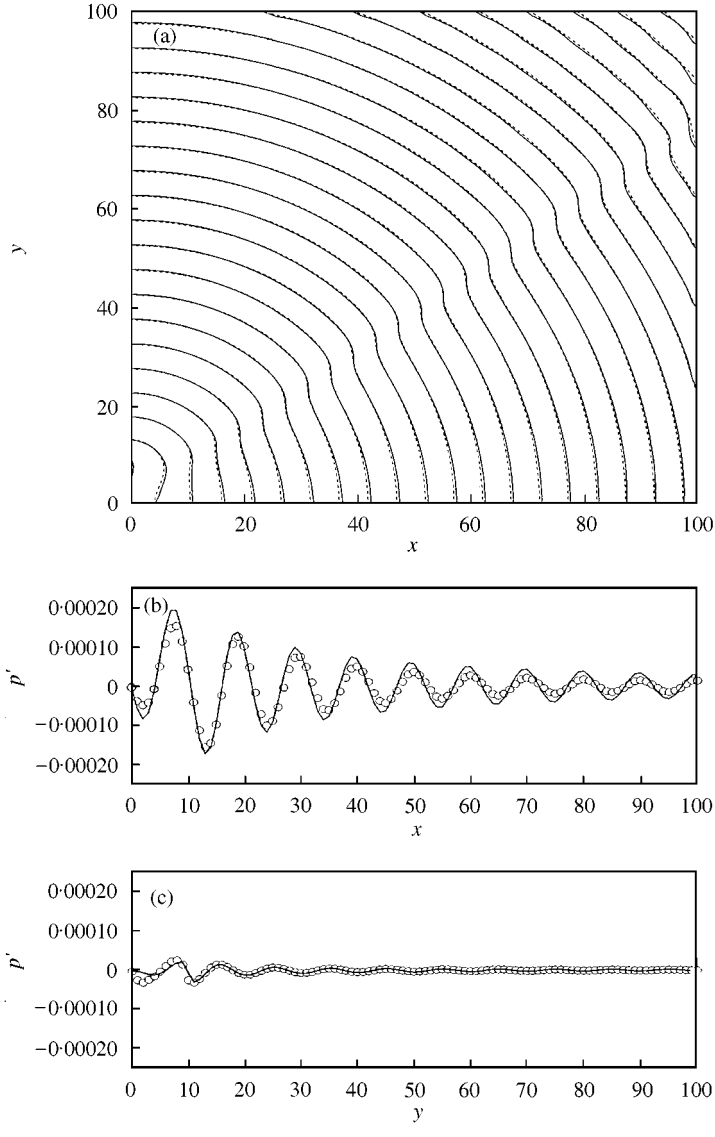

Figure 5. Solutions of axisymmetric linear acoustic wave propagation and radiation by third order ENO scheme ($t/\Delta t = 450$): (a) Pressure contour (——, numerical; · · · · · ·, analytic); (b) pressure fluctuation plot along the x-axis ($y = 0$); (c) pressure fluctuation plot along the y-axis ($x = 0$), ○, numerical (ENO3); ——, analytic.

5. RESULTS AND DISCUSSION

5.1. GRID SYSTEM AND DYNAMICS OF A PISTON AND A VALVE

The radiation of intake noise from an internal combustion engine is calculated numerically by simulating the intake stroke of axisymmetric model having a single moving cylinder and a single moving intake valve as shown in Figure 6. Mesh system consists of four blocks, deforming mesh block in cylinder, creating–removing mesh block of shade region, and non-moving blocks of duct and radiation field. The interpolation is applied to only the creating and removing block so it was possible to minimize the interpolation error. Moreover, it enabled to increase the time step. The computational grid system is composed

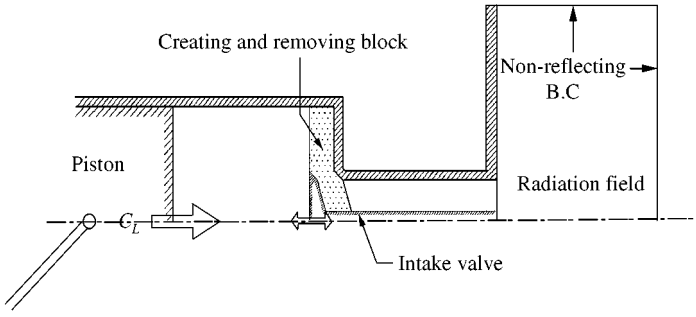

Figure 6. Schematic diagram of the model engine problem for intake noise.

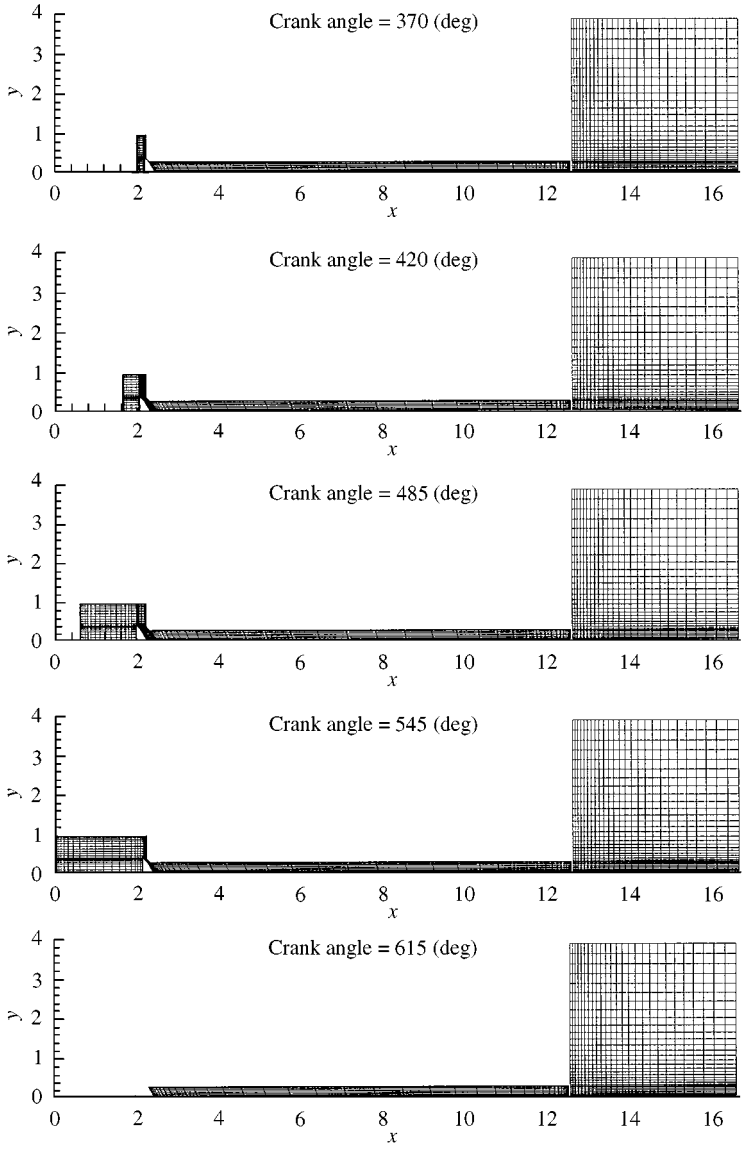

Figure 7. Moving grid system during the intake stroke.

TABLE 1

Operating characteristics of the model engine

Bore diameter (mm)	80·0
Valve diameter (mm)	33·0
Duct diameter (mm)	30·0
Duct length (mm)	385·0
Connecting rod length (mm)	131·9
Stroke (mm)	79·5
Compression ratio	9·4
Maximum valve lift (mm)	9·4
Intake valve open (deg)	16° BTDC
Intake valve closed (deg)	52° ABDC
Running condition (r.p.m.)	4500

of an in-cylinder block of 21×25, an interpolation block of $37 \times 4-20$ (which is creating–removing block), a duct block of 39×13 and a radiation field block of 28×37. To simulate the periodic motion of the piston and the valve, a moving mesh system is used as shown in Figure 7. The velocity of piston is formulated as follows:

$$S_p/\bar{S}_p = \pi/2 \sin\theta\left[1 + \frac{\cos\theta}{(R^2 - \sin^2\theta)^{1/2}}\right],$$
$$\bar{S}_p = 2LN, \quad R = l/a, \tag{23}$$

where N is the rotation number per second, L is the stroke and l is the length of the connecting lod. The intake valve is opened on 16° before top dead center (BTDC) and is also closed on 52° after bottom dead center (ABDC) and valve's dynamics is based on the sine curve. The main dimensions of the model engine are reported in Table 1.

5.2. INITIAL AND BOUNDARY CONDITIONS

In order to solve unsteady compressible Navier–Stokes equation by the numerical schemes described in the previous section, an initial condition must be prescribed. The initial conditions are set to be atmospheric pressure, atmospheric density, and zero velocity all over the computational domain. In the case of a real engine, pressure in the cylinder is a little higher than that near the valve after exhaust stroke, so the non-physical numerical wave contaminates the solution during one cycle simulation. In the case of numerical calculation, oscillating wave in the duct remains after one-cycle simulation, therefore two-cycle simulation is performed. In our study, the initial conditions at the duct and at the radiation field during the second-cycle simulation were set to be first-cycle simulation data.

No-slip boundary conditions at the wall, symmetric conditions at the axisymmetric line, and non-reflecting conditions at the radiation field are used. For the vortex flow not to cross the non-reflecting boundary, the exit zone is used in the radiation field.

5.3. COMPRESSION WAVE PROPAGATION IN THE DUCT

Figure 8 shows a three-dimensional view of the pressure contours and mesh system during the intake stroke. As the crank angle is 580°, it is obviously shown that the intake

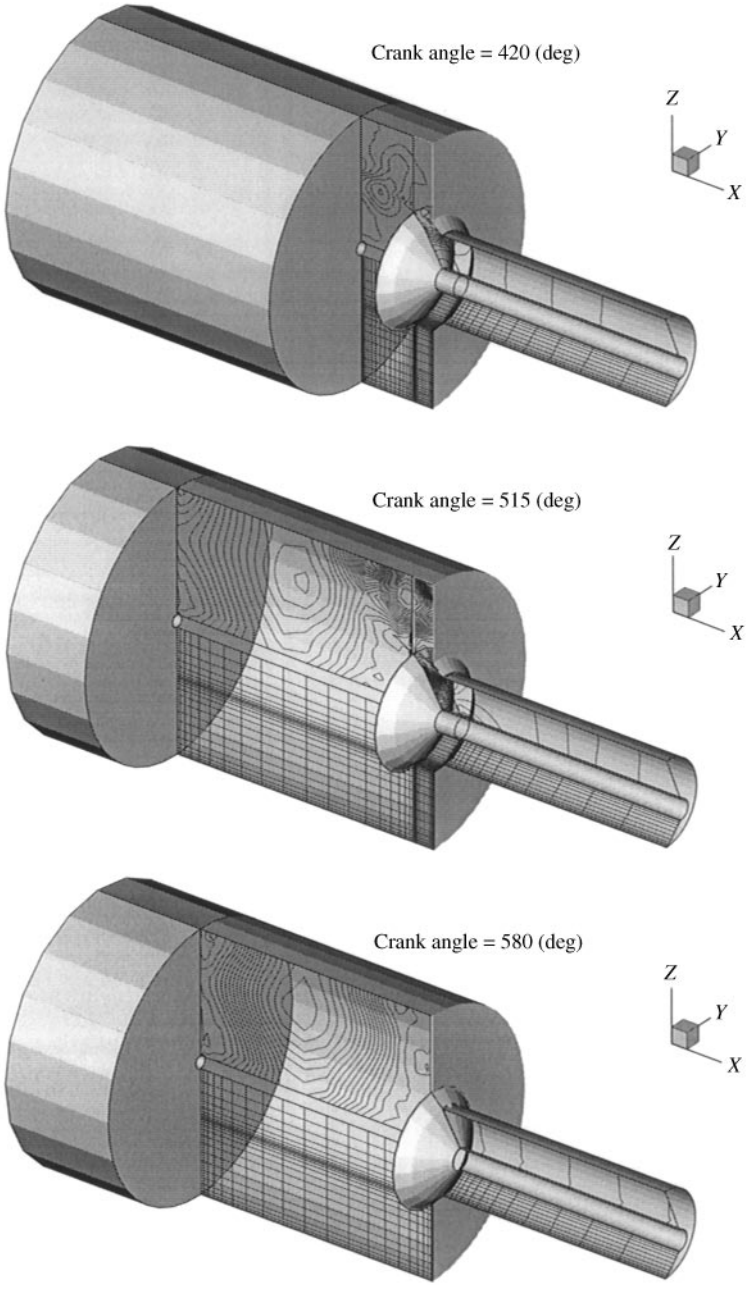

Figure 8. Three-dimensional view of the pressure contours showing perfect closing of the intake valve.

valve is perfectly closed. At the early stage, the intake valve is opened at 344° and the piston moves up to the TDC (top dead center—360°), compression wave propagates through the duct. As the piston moves down, fluid begins to be drawn into the cylinder. In the cylinder, especially near the valve, complicated vortex flows are developed. As the fluid moves down, the duct is abruptly halted after the intake valve is closed at 592°, its kinetic energy is

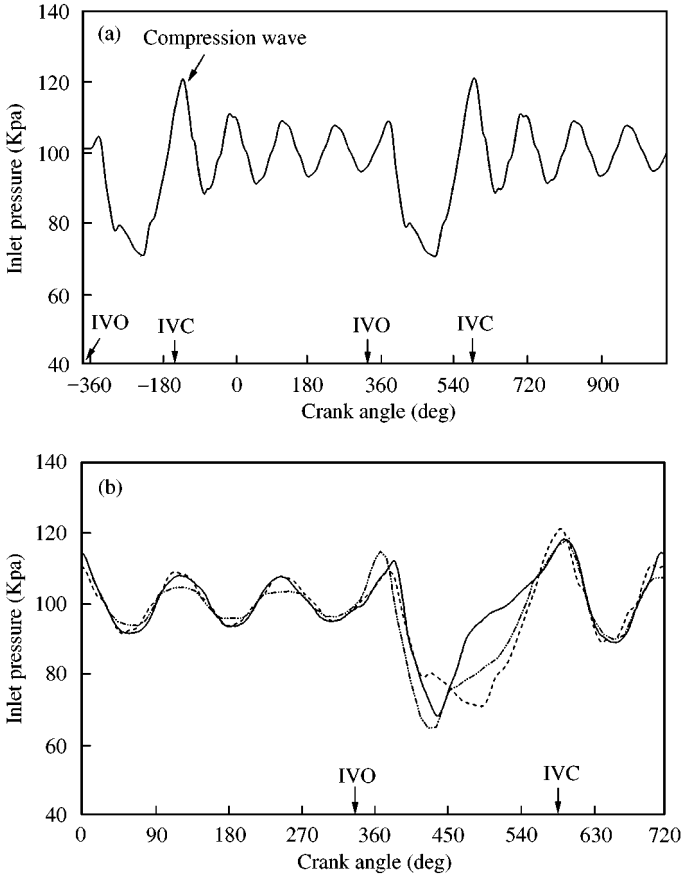

Figure 9. (a) Time history of the pressure wave in the duct during two-cycle simulation (ENO3). (b) Comparison of the in-duct pressure between the measured data and calculated data: ——, measured data; –·–·–·–·–, Lax–Wendroff (1-D); - - - - - - -, Present (ENO3-axisymmetric).

converted into a large pressure surge (compression wave), which is clearly shown as a compression wave in Figure 9(a). The comparison of the in-duct pressure between measured data and calculated data at the middle of the duct is shown in Figure 9(b). Some part of the compression wave is reflected at the open duct end and propagates to the intake valve as an expansion wave. Also, this expansion wave is reflected at the intake valve as a compression wave repetitively. Showing this phenomenon, its amplitude oscillates in the duct and decays as time elapses. Figure 9(b) shows a fair agreement of the present calculated data with the measured data. Moreover, an oscillating duct pressure is exactly the same. An underestimation in one-dimensional calculation seems to be caused by the unphysical duct end boundary condition [9]. As shown in Figure 12, a flow separation is generated by the flow that is drawn into the duct from the radiation field. This separation causes a pressure drop in the duct. So, it is difficult to apply an accurate boundary condition to the duct end boundary in the one-dimensional calculation. However, in the region of intake valve closing, the present axisymmetric and one-dimensional results are similar but do not agree with the measured data. It is estimated that this discrepancy is due to the three-dimensional effect such as valve inlet geometry.

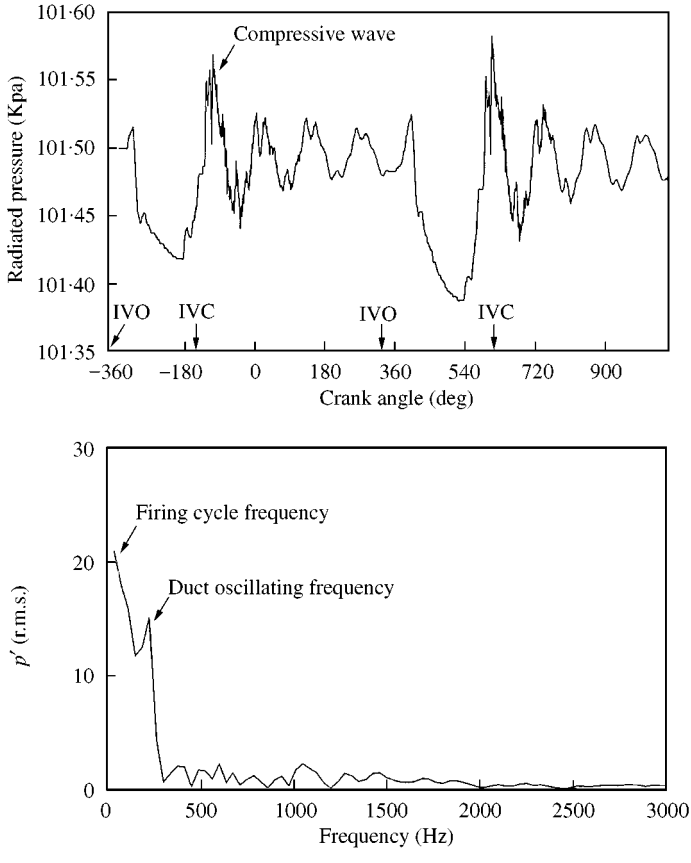

Figure 10. (a) Time history of the radiated pressure. (b) Frequency spectrum.

5.4. RADIATED SOUND FROM THE INTAKE DUCT

It is shown that a part of the compression wave inside the duct radiates with relatively large amplitude as shown in Figure 10, which is estimated at a non-dimensional position ($x = 14$, $y = 1{\cdot}5$). This is one of the main noise sources for the intake stroke. As shown in Figure 10(a), first- and second-cycle simulation results are somewhat different. During the second-cycle simulation, the radiated pressure is more expanded because the expansion wave reflects to the intake valve when the piston moves down. This phenomenon is good from a volumetric efficiency point of view but it is not good from a radiated sound pressure. In Figure 9(a), it is not definitely shown because the flow pressure is high compared with the radiated sound pressure. Figure 10(b) shows a firing cycle frequency (4500/60/2 rev = 37·5 Hz) at the running condition of 4500 r.p.m., and duct-oscillating frequency is 225 Hz approximately. This frequency definitely shows that a compression wave propagates through the duct and radiates to the far field with the speed of sound. A compression wave propagates and reflects as an expansion wave at the open duct, an expansion wave reflects as an expansion wave at the valve and an expansion wave reflects as a compression wave at the open duct. So a compression wave experiences four travels through the duct and this propagation velocity is obviously the speed of sound of 346 m/s (38·5 cm $\times$ 4 $\times$ 225 Hz) approximately. In Figure 11, it is clearly shown that the sound pressure is radiated to the far

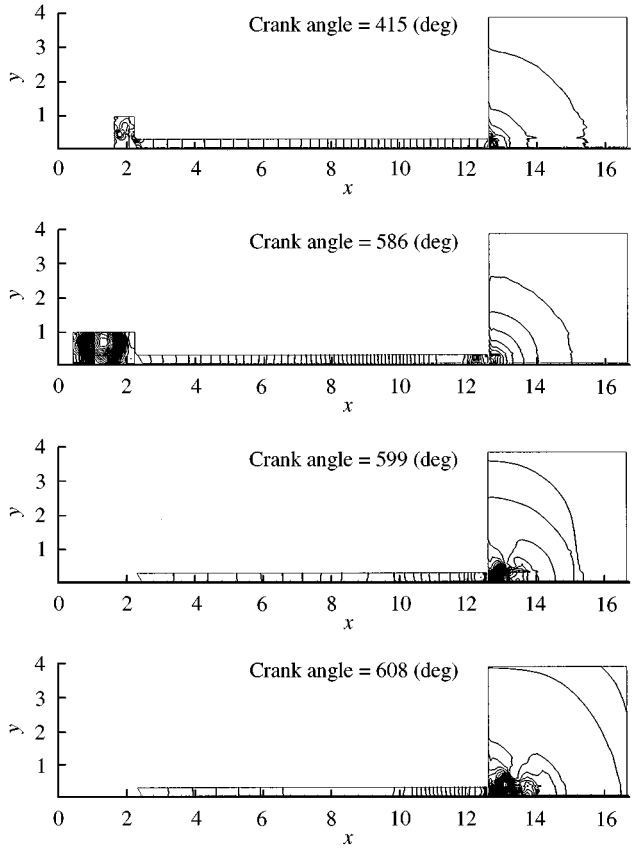

Figure 11. Pressure contours showing radiation of the expansion and compression wave to the far field (contour plot in the cylinder and duct: $p - p_0$, at the radiation fields: $(p - p_0) \times 10$, $p_0 = 101$ kPa).

fields interacting with a vortex flow at the crank angle of 608°. In Figure 12, on closing the intake valve separation flows are developed in the duct and vortex flows are generated at the radiation field. The waveforms in Figure 10(a) are similar to pressure forms in the duct. However, rapid fluctuations are different, which is relating to the vortex flows interacting with the compression wave at the radiation fields.

6. CONCLUSIONS

With a simple geometric model, it was found that the major noise source of the intake stroke was the pressure surge (compression wave), which is generated after intake valve closing. The pressure surge that was converted by fluid's kinetic energy propagates and radiates with a relatively large amplitude. Some part of the pressure surge is reflected at the open duct end and a part of it is radiated to the far field. So, its amplitude oscillates in the duct and decays as time passes.

Unsteady deforming mesh algorithm with Lagrange interpolation was suitably applied to the periodic motion of the piston and the valve. This enabled to change the number of meshes, so it could help in simulating the motion of the perfect closing of the valve.

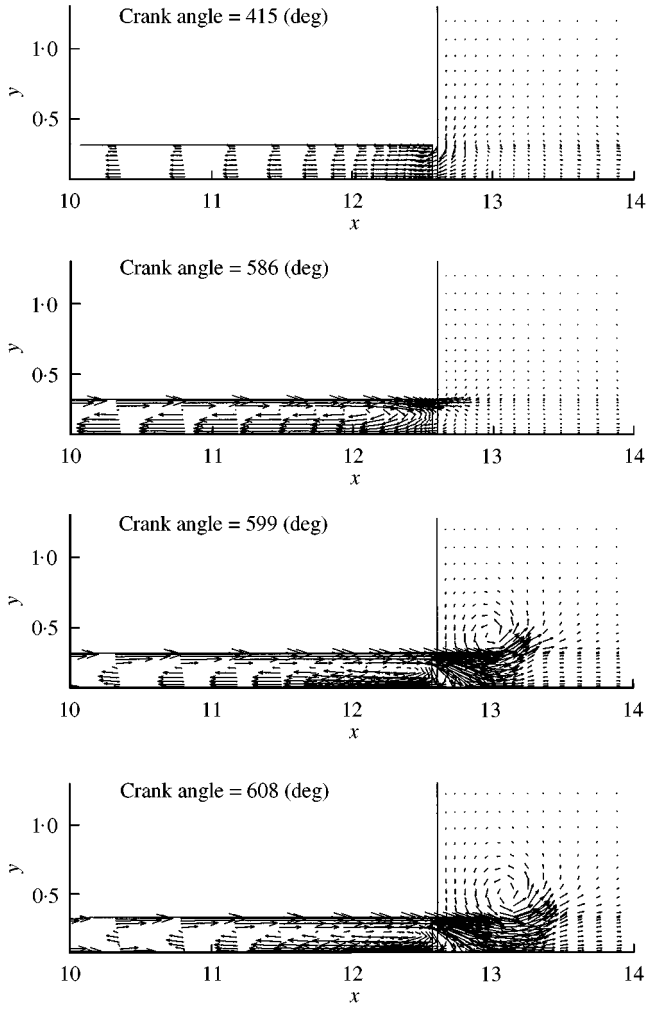

Figure 12. Velocity vector plots at some instants of the intake stroke.

In order to resolve the small amplitude waves at the radiation field, third order accurate essentially non-oscillatory (ENO) schemes were used. The characteristic non-reflecting boundary conditions were employed well for the ENO schemes to present high-quality numerical solutions.

A comparison was given between the present calculated data and measured data for in-duct pressure with satisfactory results.

REFERENCES

1. E. K. BENDER and A. J. BRAMMER 1975 *Journal of the Acoustical Society of America* **58**, 22–30. Internal-combustion engine intake and exhaust system noise.
2. Y. NISHIO, T. KOHAMA and O. KURODA 1991 *Society of Automotive Engineers Paper No.* 911042. New approach to low-noise air intake system development.
3. A. D. JONES 1984 *Noise Control Engineering Journal* **23**, 12–31. Modeling the exhaust noise radiated from reciprocating internal combustion engines-A literature review.

4. J. S. LAMANCUSA and K. B. TODD 1989 *Journal of Vibration, Acoustics, Stress, and Reliability in Design* **111**, 199–207. An experimental study of induction noise in four-cylinder internal combustion engines.
5. F. PAYRI, A. J. TORREGROSA and M. D. CHUST 1996 *Journal of Sound and Vibration* **195**, 757–773. Application of MacCormack schemes to I.C. engine exhaust noise prediction.
6. K. R. MEADOWS, D. A. CAUGHEY and J. CASPER 1993 *American Institute of Aeronautics and Astronautics Paper* 93-4329. Computing unsteady shock waves for aeroacoustic applications.
7. J. Y. YANG 1991 *American Institute of Aeronautics and Astronautics Journal* **29**, 1611–1618. Third-order nonoscillatory schemes for the Euler equations.
8. D. K. KO and D. J. LEE 1998 *Computational Fluid Dynamics Journal* **6**, 519–526. Development of an efficient fourth-order non-oscillatory scheme for compressible flows.
9. C. CHEN, A. VESHAGH and F. J. WALLACE 1992 *Society of Automotive Engineers Paper No.* 921734. A comparison between alternative methods for gas flow and performance prediction of internal combustion engines.
10. H. C. YEE 1989 *NASA TM*101088. A class of high-resolution explicit and implicit shock-capturing method.
11. T. H. PULLIAM and D. S. CHAUSSEE 1981 *Journal of Computational Physics* **39**, 347–363. A diagonal form of an implicit approximate-factorization algorithm.
12. K. MASTUNO 1992 *American Institute of Aeronautics and Astronautics Paper* 89-1992-CP. A time accurate iterative scheme for solving the unsteady compressible Navier–Stokes equations.
13. K. W. THOMPSON 1987 *Journal of Computational Physics* **68**, 1–24. Time dependent boundary conditions for hyperbolic systems.
14. K. W. THOMPSON 1990 *Journal of Computational Physics* **89**, 439–461. Time dependent boundary conditions for hyperbolic systems II.
15. T. J. POINSOT and S. K. LELE 1992 *Journal of Computational Physics* **101**, 104–129. Boundary conditions for direct simulations of compressible viscous flow.
16. J. W. KIM and D. J. LEE 1997 *Journal of Computational Acoustics* **5**, 177–191. Implementation of boundary conditions for optimized high-order compact schemes.